



HAL
open science

Ab initio informed yield criterion across body-centered cubic transition metals

Baptiste Bienvenu, Lucile Dezerald, David Rodney, Emmanuel Clouet

► To cite this version:

Baptiste Bienvenu, Lucile Dezerald, David Rodney, Emmanuel Clouet. *Ab initio* informed yield criterion across body-centered cubic transition metals. *Acta Materialia*, 2022, 236, pp.118098. 10.1016/j.actamat.2022.118098 . cea-03714226

HAL Id: cea-03714226

<https://cea.hal.science/cea-03714226>

Submitted on 5 Jul 2022

HAL is a multi-disciplinary open access archive for the deposit and dissemination of scientific research documents, whether they are published or not. The documents may come from teaching and research institutions in France or abroad, or from public or private research centers.

L'archive ouverte pluridisciplinaire **HAL**, est destinée au dépôt et à la diffusion de documents scientifiques de niveau recherche, publiés ou non, émanant des établissements d'enseignement et de recherche français ou étrangers, des laboratoires publics ou privés.

Ab initio informed yield criterion across body-centered cubic transition metals

Baptiste Bienvenu^a, Lucile Dezerald^b, David Rodney^c, Emmanuel Clouet^{a,*}

^a *Université Paris-Saclay, CEA, Service de Recherches de Métallurgie Physique, F-91191 Gif-sur-Yvette, France*

^b *Institut Jean Lamour, CNRS UMR 7198, Université de Lorraine, F-54000 Nancy, France*

^c *Institut Lumière Matière, Université Lyon 1 - CNRS, Villeurbanne, F-69622, France*

Abstract

Plasticity of body-centered cubic (bcc) metals is atypical at low temperatures, caused by the important lattice friction of $1/2\langle 111 \rangle$ screw dislocations. In this paper, we present a yield criterion that can be used to predict yield stress and active slip systems in all bcc transition metals for any applied stress. The criterion is fully parametrized on *ab initio* calculations of $1/2\langle 111 \rangle$ screw dislocation glide properties, and is applied in the case of uniaxial loading to compare with tension and compression experiments at low temperature. The criterion describes most of the different plastic behaviours observed experimentally in different metals, *i.e.* the dependence of the yield stress and active slip system on the orientation of the loading axis, as well as the tension/compression asymmetry. We find that plastic yield generally occurs at lower stresses in tension than in compression but for some metals, in particular niobium, there are large regions of the stereographic projection where compression is easier.

Keywords: Dislocations, plasticity, *ab initio*, body-centered cubic transition metals

1. Introduction

Contrary to face-centered cubic metals, plasticity in body-centered cubic (bcc) transition metals does not follow the Schmid law [1, 2]. Non-Schmid effects include a generally lower yield stress for samples subjected to tensile rather than compressive loading, and a plastic anisotropy due to the asymmetry of the bcc lattice, the so-called twinning/anti-twinning (T/AT) asymmetry. Non-Schmid effects are most pronounced at low temperature in high purity samples [1, 3–6]. In this temperature range, plasticity of bcc metals is driven by the glide of $1/2\langle 111 \rangle$ screw dislocations due to their high friction with the lattice compared to other line orientations [1, 7, 8]. These screw dislocations mainly glide in $\{110\}$ planes at low temperature [9], but glide is also observed in $\{112\}$ and $\{123\}$ planes at higher temperature [9, 10]. The T/AT asymmetry has been observed experimentally for all bcc metals

except Fe [6, 10–14]. The other major experimental deviation from the predictions of the Schmid law is the dependence of the yield stress on the sign of the applied stress, a feature known as the tension/compression (T/C) asymmetry [1, 4].

The experimentally observed features of the plastic behaviour of bcc metals have been linked to the core properties and motion of $1/2\langle 111 \rangle$ screw dislocations using atomistic *ab initio* calculations. Dezerald *et al.* [15] showed that the T/AT asymmetry originates from deviations of the screw dislocation trajectory between Peierls valleys away from the $\{110\}$ average glide plane. Kraych *et al.* [16] demonstrated that the relaxation volume tensor accounting for dislocation core dilatation and shear [17–19] varies along the trajectory, thus generating a coupling with non-glide components of the applied stress.

All physical ingredients necessary to account for the complexity and variety of non-Schmid effects, *i.e.* dislocation core trajectory and relaxation volume tensor, can be evaluated using *ab initio* calculations. Knowing these parameters, one can predict the elastic limit for any bcc metal subjected to any

*Corresponding author

Email address: emmanuel.clouet@cea.fr (Emmanuel Clouet)

mechanical loading, at zero temperature, assuming glide of $1/2\langle 111 \rangle$ screw dislocations exclusively in $\{110\}$ planes. The purpose of this article is to build such an *ab initio* yield criterion for all bcc transition metals (V, Cr, Fe, Nb, Mo, Ta, W) and to compare it to available experimental data coming from tensile and compressive tests at low temperature. Such a detailed comparison will allow to evaluate how dislocation core properties extracted from *ab initio* calculations can account for non-Schmid effects but also for variations seen experimentally between different metals.

The modeling approach has already been applied to tungsten (W) [16, 20] and chromium (Cr) [21]. These results are included here for completeness and to allow for a detailed discussion on the differences between metals.

2. Computational details and methods

2.1. *Ab initio* calculations

Calculations reported in this work were all performed within the density functional theory (DFT) with the VASP code [22]. Projector augmented wave pseudopotentials were used to model all bcc transition metals, including semi-core electrons, and the exchange-correlation potential was approximated using the GGA-PBE functional [23]. A plane-wave basis with a cutoff energy of 600 eV was used, with a k -point mesh centered on Γ with 24 points per inverse lattice parameter. Atomic relaxations were performed in simulation cells with fixed periodicity vectors until resulting forces were less than 5 meV/Å in every Cartesian direction on all atoms.

For chromium and iron, magnetism must be included [24, 25] as their 0 K ground-states are antiferromagnetic¹ (AF) and ferromagnetic (FM) respectively. For this purpose, magnetism was treated as collinear within spin-polarized DFT.

Minimum energy paths (MEP) between stable configurations were found using the nudged elastic band (NEB) method as implemented in VASP in simulation cells with fixed periodicity vectors, using 5 intermediate configurations and a spring constant of 5 eV/Å. We checked in tantalum the convergence of the properties which are the focus of this work,

¹The true experimental ground state of Cr is a spin density wave in $[100]$ direction with local AF order, but previous DFT studies [24] have shown that this complex magnetic phase is well approximated by the AF phase.

i.e. the screw dislocation trajectory and variations of the relaxation volume, with respect to the number of intermediate images used in the NEB calculation. We ran in Ta calculations considering 5 and 11 images and found only a marginal variation of the computed properties, namely a 2% variation of the Peierls stress τ_P , 3% variation on the deviation angle α^* , and a maximum variation of 10% upon all components of the variation of the relaxation volume $\Delta\Omega_{ij}$, with the results presented in Appendix B. Hence all NEB calculations presented here were done with 5 intermediate images.

2.2. Dislocation setup

$1/2\langle 111 \rangle$ screw dislocations are modeled with a dislocation dipole and fully periodic boundary conditions, using an almost quadrupolar arrangement [26, 27]. The simulation cell has periodicity vectors $\vec{p}_1 = 5/2[\bar{1}2\bar{1}] + 9/2[\bar{1}01]$, $\vec{p}_2 = 5/2[\bar{1}2\bar{1}] - 9/2[\bar{1}01]$, and $\vec{p}_3 = 1/2[111]$, containing 135 atoms per unit b along the line direction $\vec{Z} \parallel \vec{p}_3$. The glide direction \vec{X} is oriented parallel to $[\bar{1}2\bar{1}]$, and the glide plane normal is $\vec{Y} \parallel [\bar{1}01]$. A dislocation dipole of Burgers vector $\vec{b} = 1/2[111]$ is introduced in the simulation cell following anisotropic elasticity theory. Both dislocations of the dipole are displaced in opposite direction during the NEB calculations.

The dislocation setup is the same as in Refs. [20, 21]. The quadrupolar position, where both dislocations are separated by a vector $(\vec{p}_1 + \vec{p}_2)/2$, is chosen in the middle of the NEB path between the initial and final dislocation positions, thus close to the saddle point (see Fig. 1 in Ref. [21]). The plastic strain induced by the dipole in this quadrupolar position is cancelled by applying the corresponding homogeneous strain to the periodicity vectors of the simulation cell. With this choice, the initial and final configurations are exactly equivalent and have the same elastic energy. This leads to a symmetrical MEP with respect to the saddle point, as expected from symmetries of the bcc lattice.

Using the stress variations generated when both dislocations move in opposite directions in a fixed periodicity cell, one can extract the dislocation trajectory and variation of the relaxation volume tensor [16]. The stress variations $\Delta\bar{\sigma}$ are expressed as:

$$\Delta\sigma_{ij}(\xi) = \frac{C_{ijkl}}{hS} [b_k \Delta A_l(\xi) - 2h \Delta\Omega_{kl}(\xi)], \quad (1)$$

where ξ is the reaction coordinate along the NEB path, C the elastic constant tensor, $\vec{b} = a_0\sqrt{3}/2\vec{e}_z$

the Burgers vector, S the projected surface of the simulation cell in the $\{111\}$ plane, h the corresponding cell height along the $[111]$ direction, and $\Delta\bar{\Omega}$ the variation of the dislocation relaxation volume tensor. $\Delta\bar{A}$ is the variation of the dipole cut vector. If the trajectory of the $+\vec{b}$ dislocation is defined by the displacement vector $\vec{r}(\xi) = (x(\xi), y(\xi), 0)$ with $x(0) = 0$ and $y(0) = 0$, then $\Delta\bar{A}(\xi) = 2b(y(\xi), -x(\xi), 0)$. Knowing from *ab initio* NEB calculation the stress variation along the MEP, one thus obtains the dislocation trajectory and variation of the relaxation volume along the path.

The dislocation trajectory and relaxation volume extracted from Eq. 1 are very sensitive to the values of the elastic constants. Using the elastic constants of the perfect crystal, the symmetry of the trajectory and relaxation volume are not fully respected: the initial $x(0)$ and final $x(1)$ positions of the dislocations do not fall exactly at the bottom of a Peierls valley, *i.e.* the easy core configuration, and some components of the relaxation volume are not symmetrical with respect to the middle of the path. As presented in Appendix A, this can be fixed by slightly adjusting the elastic constants in order to enforce the expected symmetries. This adjustment appears legitimate, as the shear deformation produced by the dislocation dipole in the crystal induces a change of elastic constants because of anharmonicity. We checked the validity of this approach, by calculating for W [20], Cr [21] and Mo the elastic constants of a dislocated cell. The elastic constants slightly differ from the perfect crystal (up to 13% for the C_{15} and C_{44} components and less than 6% for all other constants in Cr, 18% and 15% for C_{15} and C_{44} respectively and less than 4% for all other components in Mo, and 6 and 7% for C_{15} and C_{44} respectively with less than 3% variation on all other elastic constants in W). Most importantly, the difference is of the same order as with the elastic constants obtained through the fitting procedure to enforce symmetry of the dislocation trajectory (Tab. A.2).

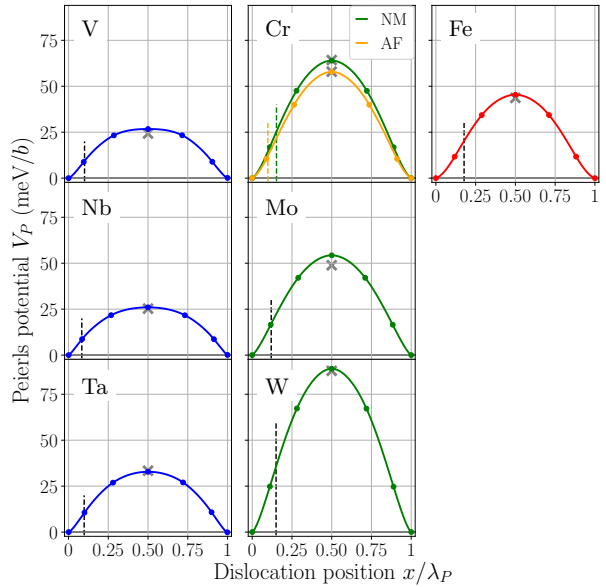
Finally, to obtain the Peierls potential V_P , the energy barriers obtained from the NEB calculations need to be corrected for the elastic energy variation caused by the change in the distance between the dislocations of the dipole when crossing the barrier. This is done using anisotropic elasticity theory with the trajectory (x, y) of the screw dislocation in the (111) plane extracted from the stress variation along the path and the modified elastic con-

stants presented in Tab. A.2 [28]. We checked the correctness of this elastic correction by comparing the height of the resulting energy barriers with additional NEB calculations where both dislocations were moved in the same direction so as to prevent large variation of the elastic energy.

3. Peierls potential and core properties

3.1. Peierls potential and trajectory

(a) Peierls potential.



(b) Trajectory in the (111) plane.

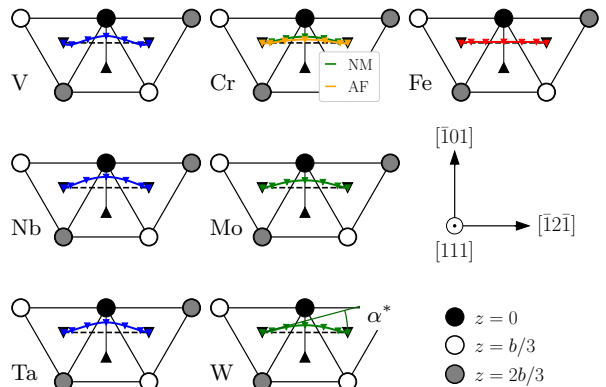


Figure 1: (a) Peierls potential V_P of the $1/2\langle 111 \rangle$ screw dislocation as a function of the dislocation position x for all bcc transition metals. Vertical lines indicate the position of the inflexion point x^*/λ_P of the Peierls potential. Grey crosses indicate the height found for the Peierls barriers when both dislocations are moved in the same direction. (b) Trajectory of the $1/2[111]$ screw dislocation gliding in a $(\bar{1}01)$ plane. Symbols are *ab initio* data after post-processing, and solid lines are quadratic splines.

Table 1: Parameters of the yield criterion for $\langle 111 \rangle \{110\}$ slip: Peierls stress τ_P (GPa), position x^* of the inflexion point of the Peierls potential (normalized by the distance λ_P between Peierls valleys), angle α^* ($^\circ$) made by the dislocation trajectory at this position, and derivatives $\Delta\Omega'_{ij}$ (\AA) of the relaxation volume tensor with respect to the position x at the inflexion point x^* .

	τ_P	x^*/λ_P	α^*	$\Delta\Omega'_{11}$	$\Delta\Omega'_{22}$	$\Delta\Omega'_{33}$	$\Delta\Omega'_{12}$	$\Delta\Omega'_P$	$\Delta\Omega'_e$
V	1.03	0.093	-14.4	-0.101	-0.096	+0.222	-0.068	+0.026	+0.004
Nb	0.79	0.047	-17.4	-0.011	-0.354	+0.423	+0.343	+0.057	-0.343
Ta	0.87	0.083	-16.2	-0.288	+0.210	+0.131	-0.095	+0.053	+0.498
Cr (NM)	2.32	0.153	-13.5	+0.025	+0.050	-0.034	+0.067	+0.041	+0.025
Cr (AF)	1.98	0.099	-7.0	-0.013	+0.116	+0.041	+0.119	+0.171	+0.103
Mo	1.40	0.114	-13.9	-0.084	+0.113	-0.008	+0.078	+0.021	+0.198
W	2.36	0.129	-14.4	-0.168	+0.239	-0.042	+0.058	+0.029	+0.406
Fe	1.65	0.143	-0.5	-0.130	+0.117	-0.029	-0.042	-0.043	+0.247

The Peierls potentials V_P after elastic correction are presented in Fig. 1.a as a function of the dislocation position x along the glide direction. The height of the barriers obtained using a setup where both dislocations of the dipole glide in the same direction, hence with negligible elastic energy variation, are indicated by grey crosses at $x = \lambda_P/2$. We note a very good agreement between both setups, highlighting the validity of the elastic correction. The obtained potentials are smooth with respect to the dislocation position and allow for the determination of the Peierls stress τ_P necessary to overcome the barrier, defined as:

$$\tau_P = \frac{1}{b} \max_x \left. \frac{\partial V_P}{\partial x} \right|_x \quad (2)$$

The values of τ_P are given in Tab. 1, and compare very well with previous results using different *ab initio* parameters, dislocation setup and definition of the dislocation position [29]. In particular, the same hierarchy of the Peierls stresses between the different bcc metals is recovered. We also note that all Peierls potentials are sharp close to the bottom of the Peierls valleys ($x = 0$ or $x = \lambda_P$) and form cusps, in contrast with the sinusoidal shape assumed in simple models [30].

The trajectories of the screw dislocation in the (111) plane are presented in Fig. 1.b, displaying the same distinctive departure from their macroscopic ($\bar{1}01$) glide plane as previously reported by Dezerald *et al.* [15, 31] using *ab initio* calculations. The deviation is quantified by the angle α^* that the trajectory makes with the ($\bar{1}01$) plane at the inflexion point x^* of the Peierls potential [20, 21] (see Tab. 1). It can be directly linked to the twin-

ning/antitwinning (T/AT) asymmetry characteristic of bcc metals [15]. A good agreement is again found with previous calculations, with the same hierarchy between bcc metals, except for Ta which was reported to have a less deviated trajectory [15]. Among all bcc transition metals, Nb has the most deviated trajectory, causing the most pronounced T/AT asymmetry, a feature also reported experimentally [12].

3.2. Variations of the relaxation volume

From the same NEB calculations as used to determine the Peierls potential and dislocation trajectory, the stress variations recorded along the paths allow to extract the variations of the relaxation volume tensor of the screw dislocation core field using Eq. 1. These variations have the following form for a screw dislocation gliding in a $\{110\}$ plane:

$$\Delta\bar{\bar{\Omega}} = \begin{bmatrix} \Delta\Omega_{11} & \Delta\Omega_{12} & 0 \\ \Delta\Omega_{12} & \Delta\Omega_{22} & 0 \\ 0 & 0 & \Delta\Omega_{33} \end{bmatrix}, \quad (3)$$

where the components $\Delta\Omega_{13}$ and $\Delta\Omega_{23}$, are zero, as previously reported for W [16, 20] and Cr [21]. The validity of this assumption was checked for all bcc metals following the method described by Kraych *et al.* [16], based on the symmetries between two NEB paths, from initial to final position, and from final to initial position. The non-zero components of the variation of the relaxation volume tensor are presented in Fig. 2 as a function of the dislocation position x for all bcc metals. Are also plotted the trace $\Delta\Omega_P$ and ellipticity $\Delta\Omega_e$ of the relaxation volume, defined as:

$$\begin{aligned} \Delta\Omega_P &= \text{Tr} \Delta\bar{\bar{\Omega}} = \Delta\Omega_{11} + \Delta\Omega_{22} + \Delta\Omega_{33} \\ \Delta\Omega_e &= \Delta\Omega_{22} - \Delta\Omega_{11} \end{aligned}, \quad (4)$$

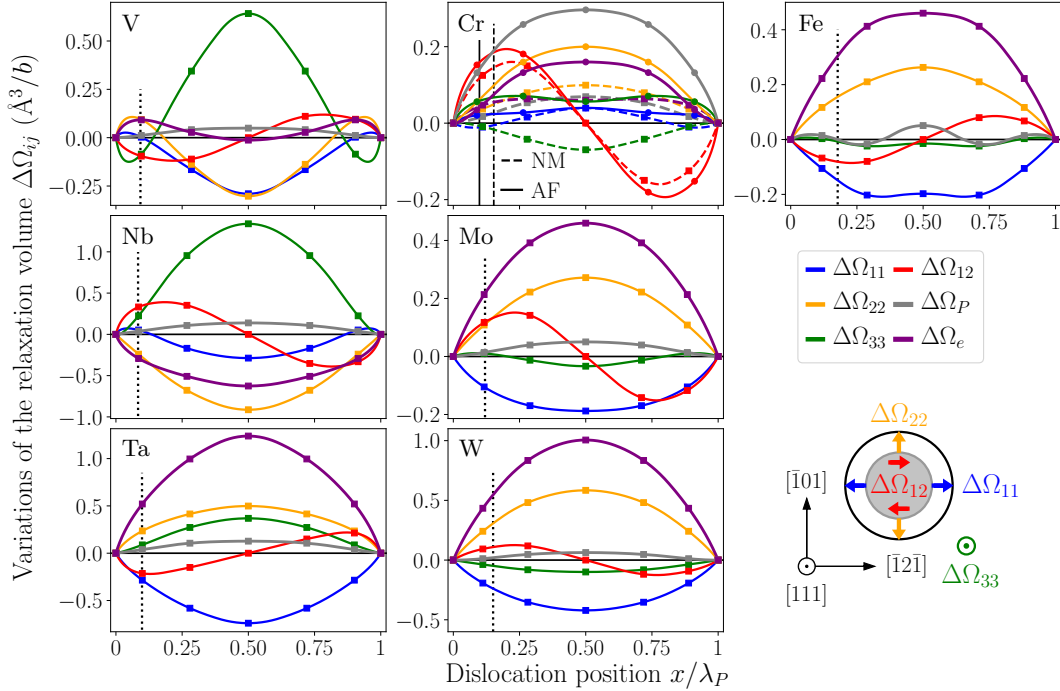


Figure 2: Variations of the relaxation volume tensor $\Delta\Omega_{ij}$ of the screw dislocation (sketched in the lower right panel) as a function of the dislocation position x in the $\{110\}$ glide plane for all bcc transition metals. Squares are *ab initio* results and lines are quadratic splines. The trace and ellipticity of the tensor are also plotted. Different scales are used depending on the metal for clarity. Vertical lines indicate the position of the inflexion point x^*/λ_P of the Peierls potential.

where $\Delta\Omega_P$ reflects the coupling with an applied pressure, and $\Delta\Omega_e$ is linked to the T/C asymmetry [16, 20].

Variations of the relaxation volume show a large variety of different behaviours among bcc metals. No group tendency can be observed: in a same column of the periodic tables, V, Nb, Ta on the one hand, Cr, Mo, W on the other hand, the same component of the relaxation volume can have different signs (see for instance $\Delta\Omega_{12}$). This makes the variations of the relaxation volume a strongly metal-dependent property. No correlation can either be found with elastic anisotropy characterized by the ratio $A = C_{44}/C'$ of shear moduli. We also note that the magnitude of the different $\Delta\Omega_{ij}$ components strongly depend on the metal, from weak variations in Cr, Mo and Fe to the large amplitudes obtained for all others, the consequence of which on the predicted yield behaviour will be discussed later.

A striking feature of the variations of the relaxation volume is that both its trace $\Delta\Omega_P$ and component $\Delta\Omega_{33}$ along the dislocation line are non-negligible for some metals. The non-zero $\Delta\Omega_{33}$

components in V, Nb, Ta and Cr imply a non-negligible effect of an applied stress σ_{33} along the dislocation line. Also, the effect of pressure, carried by $\Delta\Omega_P$, should be important in Cr, and small but non-negligible in Nb, Ta and Mo. It is thus not possible to neglect the effect of hydrostatic pressure or of a tensile stress along the dislocation line when describing non-Schmid effects, contrary to yield criteria usually used for bcc metals [32]. This motivates the use of generalized yield criteria involving all stress components [33–35].

With all core properties extracted from *ab initio* calculations, one can now write the Peierls enthalpy $\Delta H_P(x)$ of the screw dislocation gliding under an applied stress $\bar{\sigma}$ as:

$$\Delta H_P(x) = V_P(x) - \sigma_{yz} b x + \sigma_{xz} b y(x) - \sum_{ij} \sigma_{ij} \Delta\Omega_{ij}(x), \quad (5)$$

where $y(x)$ and $\Delta\bar{\Omega}(x)$ are parameterizations of the dislocation trajectory and relaxation volume along the minimum energy path for $\{110\}$ glide.

An important consequence of the relaxation volume $\Delta\bar{\Omega}$ on the yield properties of bcc metals is car-

ried by its ellipticity $\Delta\Omega_e = \Delta\Omega_{22} - \Delta\Omega_{11}$, linked to the change in the Peierls enthalpy barrier ΔH_P experienced by the screw dislocation when its glide plane is subjected to a normal stress [16] (Eq. 5). With a positive ellipticity, a glide plane subjected to a tensile stress results in a lowering of ΔH_P and thus of the yield stress. This effect was validated in W, which has a positive ellipticity: using direct *ab initio* calculations, Kraych *et al.* [16] showed a lowering of the Peierls enthalpy ΔH_P when a tensile stress was applied perpendicular to the glide plane. This behaviour matches the T/C asymmetry generally observed in bcc metals, with easier plastic yield in tension than in compression. Surprisingly, Nb and V seem to deviate from this general behaviour with $\Delta\Omega_e$ negative in Nb and almost zero in V. In particular, one expects in Nb an increase of the Peierls enthalpy ΔH_P for a glide plane in tension. We checked this prediction by performing *ab initio* calculations in Nb of the dislocation Peierls enthalpy for a non-null stress component normal to the screw dislocation glide plane. The results are presented in Fig. 3, where a stress σ_{22} is applied to the system, resulting as predicted in a lower barrier when the glide plane is in compression. Results of the model (dashed lines) are in good agreement with direct *ab initio* NEB calculations, in particular regarding the slope of the enthalpy barriers, defining the yield stress. Consequences of this peculiarity of Nb on its yield properties will be discussed in more details when comparing to experimental data.

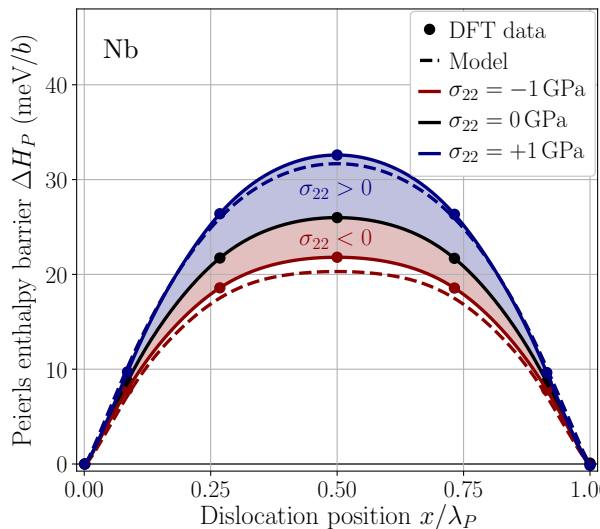


Figure 3: Peierls enthalpy barrier ΔH_P of a screw dislocation in Nb gliding in a $\{110\}$ plane subjected to a tensile or compressive stress σ_{22} of magnitude 1 GPa.

4. Uniaxial mechanical loading

4.1. Generalized yield criterion

The yield stress for any mechanical loading is defined as the stress state for which $\Delta H_P(x)$ (Eq. 5) ceases to have a saddle point. We illustrate in this section the approach by considering a uniaxial mechanical loading, *i.e.* a tension or compression test, and develop an analytical yield criterion based on the *ab initio* data obtained in the previous section. Full derivation of the model is given in more details in previous works [16, 20, 21]. The choice to focus on uniaxial loading is motivated by the availability of experimental data at low temperature for all bcc transition metals, and hence the possibility to compare the results of the presented yield criterion with experiments. However, we stress that the approach described here can be applied to any other mechanical loading. The developed yield criterion applies only at 0 K, as it ignores thermal activation. It can be extended to finite temperature, taking account of the thermally activated glide of screw dislocations through nucleation and propagation of kink-pairs using a line tension model parametrized on *ab initio* calculations [29, 36].

A uniaxial loading of magnitude σ along an axis \vec{t} defined by the angle ζ between the slip direction and \vec{t} and the angle χ between the dislocation glide plane and the maximum resolved shear stress plane (MRSSP) has the following stress tensor:

$$\sigma \begin{bmatrix} \sin^2 \zeta \sin^2 \chi & 1/2 \sin^2 \zeta \sin 2\chi & 1/2 \sin 2\zeta \sin \chi \\ & \sin^2 \zeta \cos^2 \chi & 1/2 \sin 2\zeta \cos \chi \\ & & \cos^2 \zeta \end{bmatrix} \quad (6)$$

Injecting this stress tensor in Eq. 5 gives the Peierls enthalpy barrier. The yield stress σ_Y to overcome this barrier is then found at an unstable position x^* corresponding to the inflexion point of the Peierls enthalpy barrier. In tension, the yield stress is expressed as [21]:

$$\sigma_Y^T(\zeta, \chi) = \frac{2\tau_P}{\sin(2\zeta) \frac{\cos(\chi - \alpha^*)}{\cos(\alpha^*)} + \beta(\zeta, \chi)}, \quad (7)$$

where τ_P is the Peierls stress in absence of non-Schmid effects given by Eq. 2. α^* is the angle between the tangent to the trajectory at the inflexion point x^* and the $(\bar{1}01)$ glide plane. β is a function of the angles ζ and χ and depends on the derivatives of the relaxation volumes with respect to the

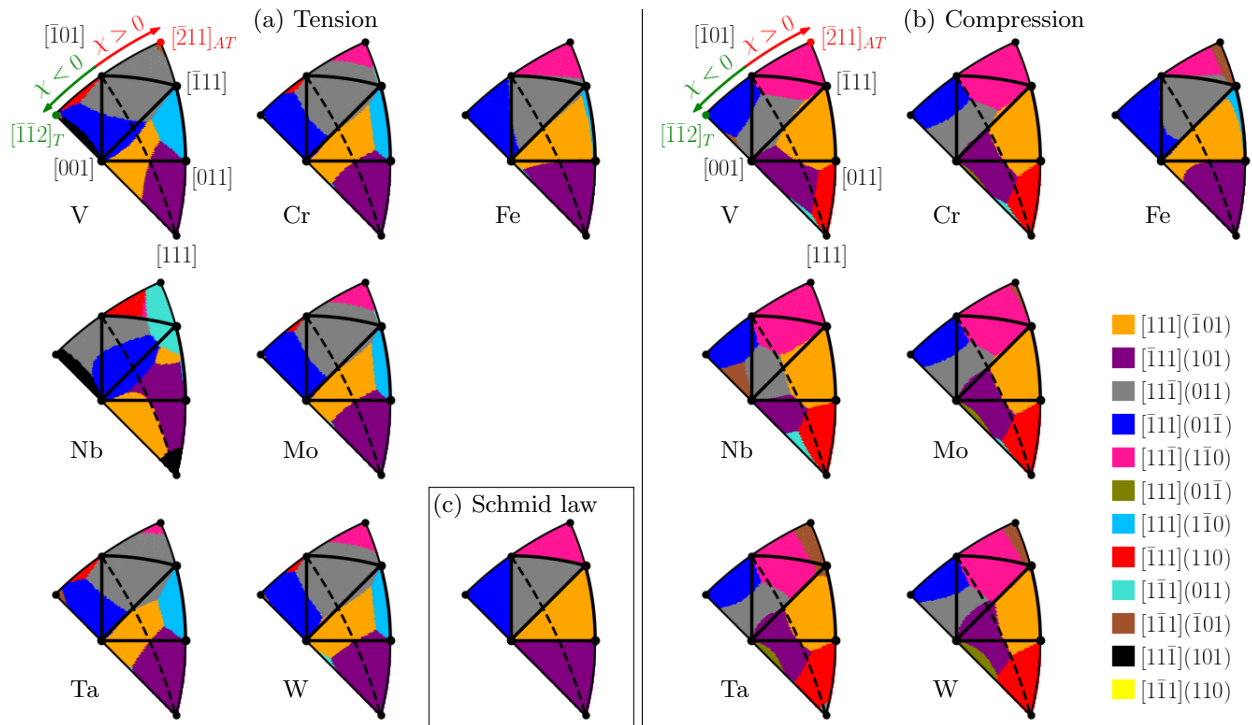


Figure 4: Predicted distribution of primary slip systems for all bcc transition metals according to the yield criterion of Eqs. 7 and 9 under uniaxial (a) tension and (b) compression. Results for Cr are presented for the non-magnetic phase. The distribution predicted by the Schmid law in either tension or compression is shown in (c), which is the same for all bcc transition metals.

position x at x^* :

$$\beta(\zeta, \chi) = \sin^2 \zeta \left[\frac{\Delta \Omega'_e}{b} \cos(2\chi) + \frac{2\Delta \Omega'_{12}}{b} \sin(2\chi) + \frac{\Delta \Omega'_P}{b} \right] - (1 - 3 \cos^2 \zeta) \frac{\Delta \Omega'_{33}}{b}. \quad (8)$$

Superscripts ' and * indicate the first derivative with respect to x and its value at x^* respectively. Details about the derivation of the yield criterion in the case of a uniaxial loading are given in Ref. [21]. Parameters of the yield criterion in tension are listed in Tab. 1 for all bcc metals. The yield criterion for compression is obtained by substituting $\chi \rightarrow -\chi$, $\alpha \rightarrow -\alpha$ and $\beta \rightarrow -\beta$ in Eq. 7, resulting in the following expression:

$$\sigma_Y^C(\zeta, \chi) = \frac{2\tau_P}{\sin(2\zeta) \frac{\cos(\chi + \alpha^*)}{\cos(\alpha^*)} - \beta(\zeta, \chi)}. \quad (9)$$

In the absence of non-Schmid effects, *i.e.* considering both a straight dislocation trajectory ($y(x) = 0$) and a constant relaxation volume ($\Delta \Omega_{ij} = 0$),

the yield stress in tension and compression is:

$$\sigma_Y^{SL}(\zeta, \chi) = \frac{2\tau_P}{\sin(2\zeta) \cos(\chi)} = \frac{\tau_P}{\text{SF}(\zeta, \chi)}, \quad (10)$$

where $\text{SF}(\zeta, \chi) = \sin(2\zeta) \cos(\chi)/2$ is the Schmid factor of the slip system. This expression results in the Schmid law, and is equivalent to Eqs. 7 and 9 with $\alpha^* = 0$ and $\beta(\zeta, \chi) = 0$.

Our generalized yield criterion differs from that first introduced by Vitek and co-authors [32, 33, 37–41] and used in various simulation works [42, 43]. As previously discussed [16], Vitek's criterion considers a mechanical loading made of a superposition of a shear stress τ in the MRSSP and a non-glide stress σ normal to the dislocation line. The obtained criterion is equivalent to the one obtained here (Eqs. 7 and 9) only when the components $\Delta \Omega_{33}$ and $\Delta \Omega_P$ of the relaxation volume can be neglected [16]. As shown in previous section, such an approximation is not valid in all bcc transition metals, thus motivating the use of a more general criterion incorporating all contributions.

4.2. Variations among bcc metals

Comparing Eqs. 7 and 9, when the effect of the relaxation volume is neglected, *i.e.* with $\beta(\zeta, \chi) = 0$, the difference between tensile and compressive yield stresses is carried by the reversed sign of the deviation angle α^* . This results essentially in reversing the "soft" twinning sense upon changing the sign of the applied stress σ . The complex dependence of the β function on the angles ζ and χ makes a qualitative comparison of behaviours in tension and compression more difficult. To better visualize the difference between tension and compression, the predicted slip activity, *i.e.* the distribution of primary slip system as a function of the orientation of the loading axis, is presented in Fig. 4 under both mechanical loadings for all bcc transition metals. These stereographic projections show the slip system with the lowest yield stress according to Eq. 7 in tension (Eq. 9 in compression) among the twelve $1/2\langle 111 \rangle \{110\}$ possible systems, similar to previously reported using different yield criteria [39–41].

As shown in Fig. 4.a and b, the predicted slip activity deviates drastically from the predictions of the Schmid law in Fig. 4.c, according to which the same single $\langle 111 \rangle \{110\}$ slip system should have the lowest yield stress in both tension and compression in any stereographic triangle delimited by axis $\langle 100 \rangle$ - $\langle 110 \rangle$ - $\langle 111 \rangle$, and should show the same distribution in all bcc transition metals. When non-Schmid effects are included, this simple distribution changes, with various coexisting primary slip systems in a same triangle. As a consequence of the deviation angle α^* , the minimum symmetry-equivalent region of the stereographic space is not just $1/48$ of the whole sphere, *i.e.* a single triangle, as obtained with the Schmid law, but $1/24$ of the sphere, *i.e.* two adjacent triangles, as observed here for any metal in both tension and compression [20, 21].

Looking at the predicted slip activity, all bcc metals show a similar distribution, except Fe and Nb. Indeed, Fe is the only metal for which a marginal deviation from the Schmid law is predicted, due to its small deviation angle and also limited variation of its relaxation volume. On the contrary, tensile and compressive slip activities in Nb show major deviations with respect to the Schmid law and also to all other metals. Most particularly, regions of the standard triangle are predicted to favor an unexpected slip system in tension, $[\bar{1}11](01\bar{1})$ in blue, and in compression, $[11\bar{1}](011)$ in grey. This is a

consequence of both a high deviation angle α^* and a large magnitude of $\Delta\Omega_{ij}$, with a negative ellipticity. Although Ta has also a high deviation angle, it does not appear as different from other metals as Nb. This difference between Nb and Ta lies in the high magnitude of the $\Delta\Omega_{33}$ component of the relaxation volume in Nb. Due to this component, yield stress in Nb is sensitive to a normal stress acting along the dislocation line. This coupling in Nb is responsible for the region in the central triangle of the stereographic projection where the $[\bar{1}11](101)$ (in purple) and $[11\bar{1}](011)$ (in grey) are predicted as primary slip systems in tension and compression respectively.

The four other metals, namely Ta, Cr, Mo and W, display similar slip activity in both tension and compression. The main features are the activity of both the expected $[111](\bar{1}01)$ (orange) slip system with $[111](\bar{1}10)$ (sky blue) in tension and $[\bar{1}11](101)$ (purple) in compression over the standard stereographic triangle.

5. Comparison with experimental data

As presented in the previous sections, the yield criterion proposed in this work, based on *ab initio* calculations of the screw dislocation properties, gives a good qualitative reproduction of known features of the yield behaviour of bcc transition metals under uniaxial loading, namely the T/AT asymmetry and a different behaviour under tension and compression. We now compare the predictions of the model with experimental data in terms of the variation of the yield stress and slip activity as a function of the orientation of the loading axis.

5.1. Yield stress and slip activity

The *ab initio* yield stresses are presented in Fig. 5 for all bcc transition metals, with experimental data measured at 77 K for different loading orientations taken from various references (see Tab. C.4). To effectively compare the predictions of the yield criterion to experiments, it is necessary to account for the variations of the yield stress with the crystal orientation as non-Schmid effects make it impossible to define a single experimental value. We therefore report for each element the range of yield stresses measured for different orientations of the loading axis and compare them with the range predicted by the model over the whole stereographic space. The *ab initio* data are reported both according to the Schmid law and including non-Schmid

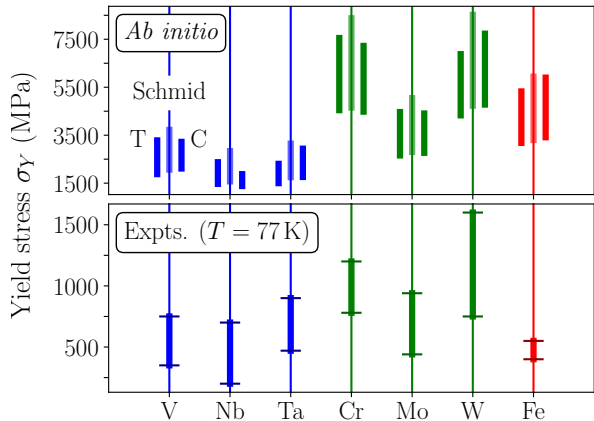


Figure 5: Comparison between the yield stress σ_Y predicted by the *ab initio* yield criterion and experimental data taken from various references at 77 K (see Tab. C.4 for values and references). Experimental yield stresses range from their minimum to maximum over the whole stereographic space in both tension and compression. *Ab initio* data are plotted both according to the Schmid law (Schmid, center bar), in tension (T, left bar), and in compression (C, right bar).

effects in tension and compression to highlight the different ranges covered by the different predicted yield stresses. We observe that deviations from the Schmid law tend to narrow the width of the yield stress distributions, with lower stresses in tension than in compression except in Nb due to the negative ellipticity discussed above.

As already largely discussed in the literature [31, 45, 46], depending on the metal, atomistic calculations overestimate the yield stress by a factor 2 to 4 with respect to experiments. This effect is not corrected by accounting for non-Schmid effects in the evaluation of the yield stress, as shown in Fig. 5, which was proposed as a possible explanation for such discrepancy in previous works [47, 48]. Several other explanations have been proposed, among which a contribution of the zero-point energy [46]. Despite this scaling effect, we note that the model reproduces the hierarchy of yield stresses between metals, except for Fe which is found experimentally to have a narrower range of variations and, on average, a lower yield stress than all other metals, a specificity which is not captured by our model. In the following, yield stresses are rescaled to focus on their relative variations with respect to the loading axis rather than their absolute values.

We first compare the results of our model with experimental data in terms of the dependence of the yield stress and slip activity on the angle χ

between the $\{110\}$ glide plane and the MRSSP. Only data measured at low enough temperature are relevant for the comparison since non-Schmid effects fade out when the temperature is increased up to the athermal temperature of the Peierls mechanism T_{ath} , where lattice friction becomes negligible [1, 20, 49]. Slip activity, *i.e.* active glide planes, is determined experimentally through the identification of slip traces left by dislocations on the surfaces of the deformed samples. The planes where the dislocations have slipped can then be defined by the angle ψ between the observed slip plane and the expected $(\bar{1}01)$ plane.

Comparison between the yield criterion in tension (Eq. 7) and experiments is presented in Fig. 6 for a constant ζ angle, *i.e.* a constant angle between the tensile axis \vec{t} and the slip direction \vec{b} , as a function of the angle χ . Experimental data were measured at 4.2 K with $\zeta \simeq 47^\circ$ for Nb [12], Mo [14] and Fe [11]. Results for V and Ta under uniaxial tension with $\zeta \simeq 50^\circ$ are presented in Fig. 7 and compared with experimental data measured at 77 K taken from Bressers *et al.* [44] for V and Nawaz and Mordike for Ta [6]. To emphasize on the sensitivity of the results on ζ , three different angles are plotted for the theoretical yield stresses.

The presented yield stress profiles highlight the departure from the Schmid law, characterized by the T/AT asymmetry and a strong competition between slip systems. According to the Schmid law, only the $[111](\bar{1}01)$ system (orange) is expected over the range of orientations contained in the standard stereographic triangle delimited by axis $[001]$ - $[011]$ - $[\bar{1}11]$, resulting in $\psi(\chi) = 0$ for all χ angles. This is the case for Fe only (Fig. 6.c), for which non-Schmid effects have a marginal impact. In the range of ζ angles considered here, we report a very good agreement with experimental data for Mo and Fe (Fig. 6.b and c) in terms of both relative variation of the yield stress and active slip systems. The agreement for Nb is less satisfying, especially for $\chi < 0$, with a steep decrease of the yield stress not reproduced by the model. This corresponds to the region of the stereographic triangle where anomalous slip was reported experimentally [12]. Recent TEM observations and atomistic simulations have proposed that such anomalous slip involves highly mobile multi-junctions between screw dislocations [50]. This effect can therefore not be understood from the glide properties of single dislocations, as considered in the present model. Regarding the predicted slip activity in Nb, the exper-

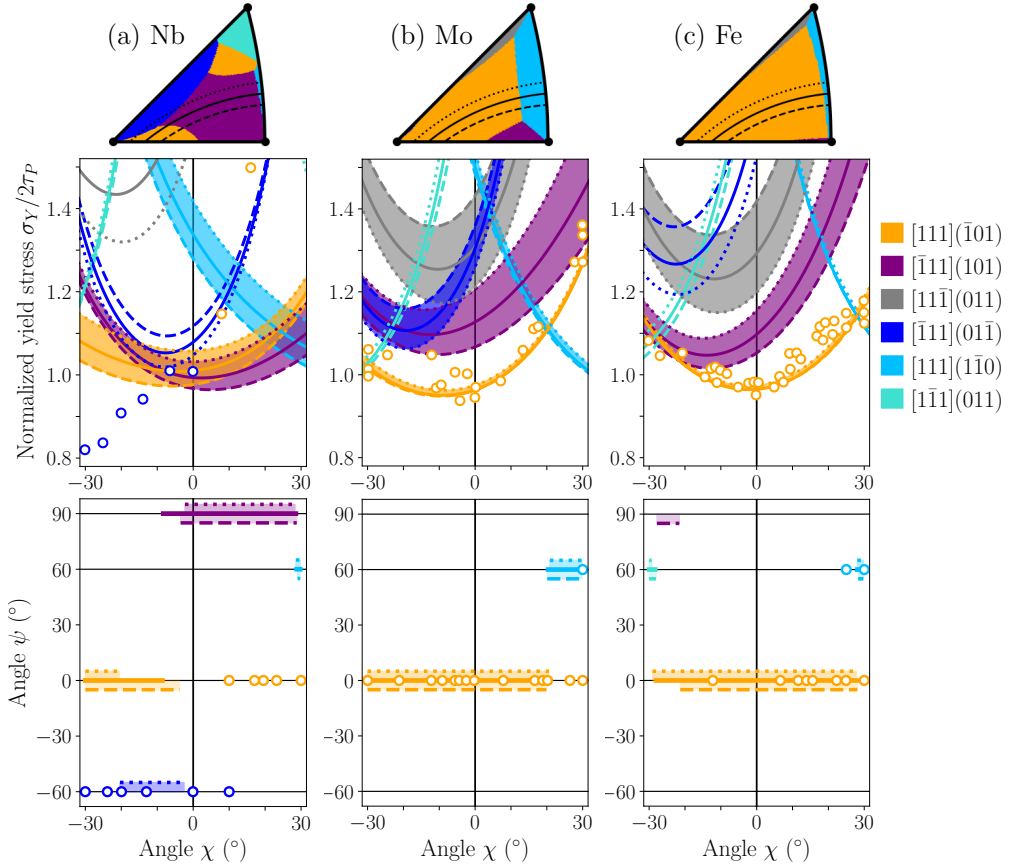


Figure 6: (Middle row) Normalized yield stress σ_Y/σ_Y^0 under uniaxial tension for each $\{111\}\{110\}$ slip system as a function of the angle χ for (a) Nb, (b) Mo, and (c) Fe along the $\zeta \in \{45^\circ; 48^\circ; 51^\circ\}$ lines shown in black in the stereographic triangles of the upper row. (Lower row) Corresponding angle ψ between the observed and the expected $(\bar{1}01)$ slip plane. Profiles for the three ζ -lines are shifted up and down for clarity. Experimental data in tension (open symbols) for both σ_Y and the angle ψ were measured for $\zeta \simeq 47^\circ$ at 4.2 K for both Nb [12], Mo [14] and Fe [11]. Experimental σ_Y are normalized by 600 MPa, 1100 MPa and 740 MPa for Nb, Mo and Fe respectively, and predicted σ_Y by $2\tau_P$ (see Tab. 1), which is the lowest value predicted by the Schmid law when the Schmid factor of the slip system is maximum (0.5).

imental $[\bar{1}11](01\bar{1})$ system (blue, with $\psi = -60^\circ$) is also predicted by the model for $\chi < 0$. In the $\chi > 0$ range, the authors report activity of the expected $[111](\bar{1}01)$ slip system (orange, with $\psi = 0$), while the model predicts slip in the $[\bar{1}11](101)$ system (purple, with $\psi = 90^\circ$). In terms of the yield stress, very few experimental yield stresses were measured by the authors for $\chi > 0$, not allowing for a proper comparison with the predictions of the model.

Experimental slip activity measured for single crystals of V [44] and Ta [6, 51, 52] under uniaxial tension and compression at 77 K revealed wavy slip lines for many orientations. In Fig. 7, we retained only those orientations for which a precise slip system was determined. A good agreement between predictions of the model and experiments is found

for V, both in terms of yield stress and slip activity, except for $\chi > 20^\circ$ where the observed $[111](\bar{1}10)$ slip system (sky blue, with $\psi = +30^\circ$) is predicted to require a lower yield stress than observed experimentally. The same applies for Ta, for which the predicted slip activity in tension is similar to V, showing a satisfying agreement in terms of the predicted relative variations of the yield stress. Very few experimental points are available in terms of slip activity in the same reference, caused by the temperature effect discussed above. Still, the predicted $[111](\bar{1}01)$ slip system (orange, with $\psi = 0$) for $\chi > 0$ is also observed experimentally, and is predicted over the entire range of χ angles, except for $\chi > +15^\circ$ where slip is predicted in the $[111](\bar{1}10)$ system (sky blue, with $\psi = +30^\circ$).

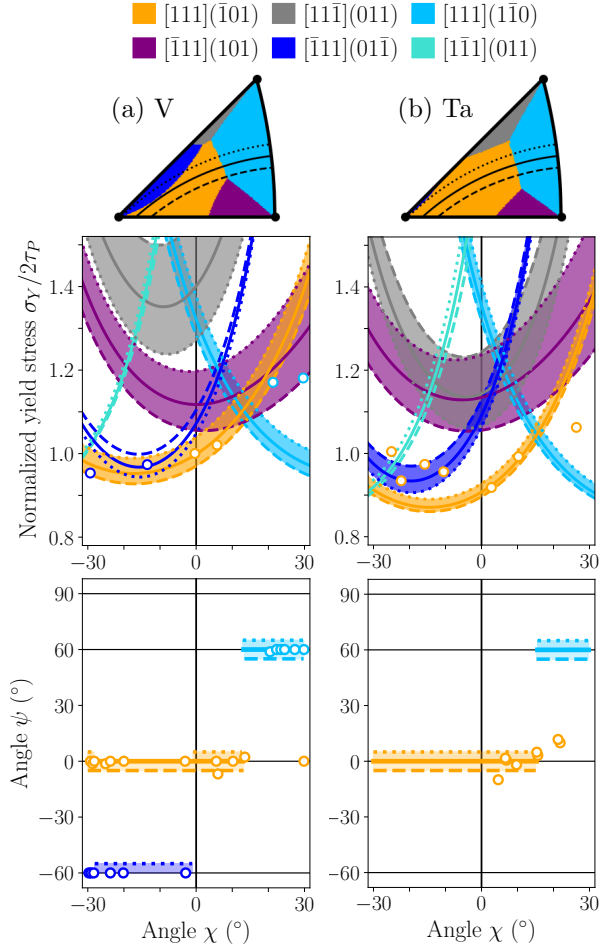


Figure 7: Normalized tensile yield stress and angle ψ along the $\zeta \in \{48^\circ; 51^\circ; 54^\circ\}$ lines for (a) V and (b) Ta. Notations are the same as in Fig. 6. Experimental tensile data (open symbols) were measured at 77 K for $\zeta \simeq 50^\circ$ for both V [44] and Ta [6]. Experimental yield stresses are normalized by 500 and 510 MPa for V and Ta respectively.

5.2. Tension/compression asymmetry

We now focus on discussing the asymmetry between tension and compression, comparing again predictions of the model with experimental data. A tension/compression (T/C) asymmetry has been observed experimentally in all bcc metals under uniaxial loading, over a wide range of crystal orientations [1, 4, 61]. In particular, the yield stress of bcc metals is generally lower in tension than in compression considering the same loading axis.

In this section, the T/C asymmetry is analyzed as a function of the loading axis using the strength differential (SD) introduced by Gröger *et al.* [38, 39] in their simulation work on Mo and W, and which

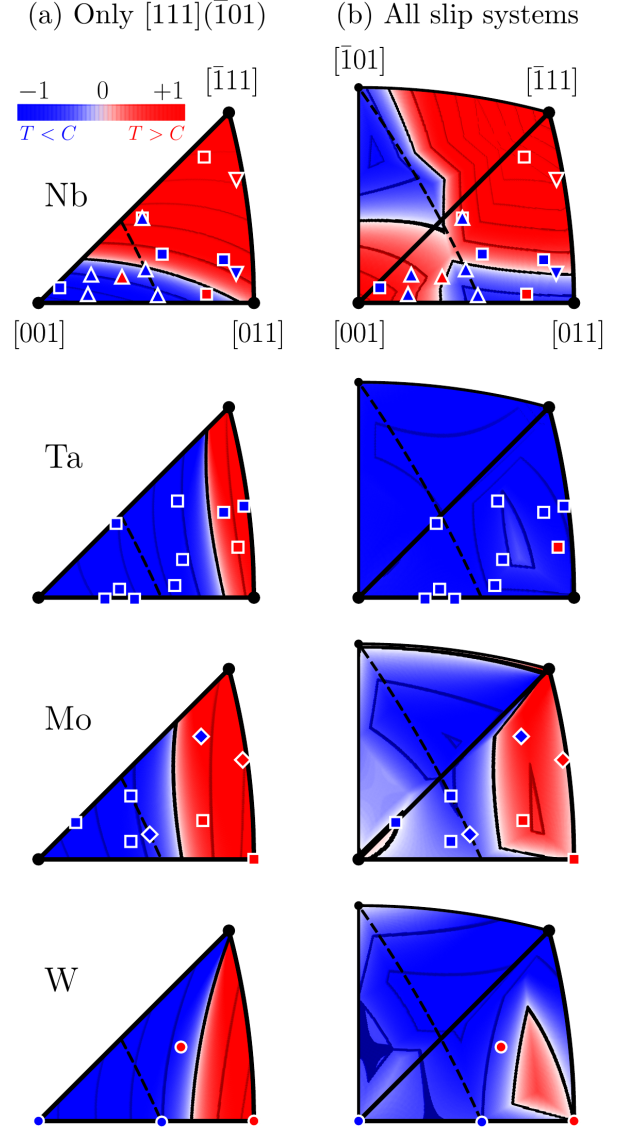


Figure 8: Strength differential (Eq. 11) of Nb, Ta, Mo, and W single crystals under uniaxial loading of (a) only the $[111](\bar{1}01)$ slip system, and (b) all $\langle 111 \rangle \{110\}$ slip systems. Experimental data at 77 K are indicated by colored squares (for Nb [53, 54], Ta [6, 55] and Mo [56, 57]), at 123 K by diamonds (for Mo [58]), at 158 K by upwards triangles (for Nb [59]), at 228 K by downwards triangles (for Nb [54]), and at 293 K by circles (for W [60]). Levels are indicated by dark lines every 0.1 step.

is expressed as the following:

$$SD = \frac{\sigma_T - \sigma_C}{(\sigma_T + \sigma_C)/2}, \quad (11)$$

where σ_T and σ_C are the absolute values of the yield stress in tension and compression respectively.

Level plots of SD are presented in Fig. 8 for Nb, Ta, Mo, and W. Only these four metals are presented as experimental data at low enough temperature is not available for other metals. Data for Nb, Mo and Ta were mostly measured at 77 K, which is below the athermal temperature T_{ath} of the Peierls mechanism (between 300 and 400 K), and at 293 K for W, also below T_{ath} (around 700 K). Experimental values for T_{ath} are summarized in Tab. C.4. Other experimental data comparing tensile and compressive behaviours are available for Fe, Nb, Mo, Ta, and V but were all measured at least at room temperature, which is too close to T_{ath} for these metals. Results for V, Cr and Fe where experimental data are missing are given in Supplementary Materials. Results of Fig. 8 are plotted considering only the primary expected slip system $[111](\bar{1}01)$ in the left column, and all $\langle 111 \rangle \{110\}$ slip systems in the right column, in order to stress the importance of accounting for all possible systems when describing the T/C asymmetry.

When only the $[111](\bar{1}01)$ slip system is considered, all bcc metals presented in Fig. 8 show a non-negligible range of loading orientations for which compression activates slip more easily than tension (*i.e.* $SD > 0$, in red). This is a direct consequence of the T/AT asymmetry of the $[111](\bar{1}01)$ slip system. Upon changing the sign of the applied stress (*i.e.* from $\sigma > 0$ in tension to $\sigma < 0$ in compression), the twinning region is reversed from $\chi < 0$ in tension, to $\chi > 0$ in compression. Hence, the yield stress is lower in compression than in tension near the $[011]-[\bar{1}11]$ edge of the standard stereographic triangle, and the opposite near the $[001]$ axis. In Mo and Ta, a small region where compression is easier than tension is predicted only in the part where $\chi > 0$. The location of this region is in qualitative agreement with experiments. However, this reasoning is too simplistic as active slip systems may differ inside the standard triangle when non-Schmid effects are accounted for. For this reason, it is necessary to take all possible $\langle 111 \rangle \{110\}$ slip systems into account to have a correct representation of the T/C asymmetry and to compare with experiments. Two adjacent triangles are then plotted to describe the minimum symmetry-equivalent region of the stereographic projection.

When all slip systems are considered, the range of orientations where compression is easier than tension gets narrowed for Ta and W, while a similarly large or even wider range is observed for Nb and Mo. For Ta, the predicted yield stress is lower in

tension than in compression for all orientations of the loading axis, in good agreement with experimental data [6, 52, 55], except near the $[011]-[\bar{1}11]$ edge. In this region, the authors report a lower compressive yield stress, not predicted by the model. Ta has the most pronounced T/C asymmetry in favor of tension among the four metals in Fig. 8, a consequence of the high positive magnitude of the ellipticity component $\Delta\Omega_e$ of its relaxation volume (see Tab. 1 and Fig. 2).

The reverse effect is observed for Nb, for which the T/C asymmetry is predicted to be the most pronounced in favor of compression. A striking feature of this asymmetry in Nb is the lower compressive stress found for orientations near the center of the standard stereographic triangle, however comparing poorly with experimental data in this region. A large range of orientations close to the $[\bar{1}11]$ and $[001]$ corner orientations show a lower compressive yield stress, comparing well with experimental data close to $[\bar{1}11]$, but poorly near $[001]$. In this last region, corresponding to $\chi < 0$, all authors reported anomalous slip for samples deformed in either tension and compression, which cannot be captured by the presented model, and have an impact on both the slip activity and the yield stress.

6. Conclusion

Following previous theoretical developments [15, 16], the Peierls stress of the $1/2\langle 111 \rangle$ screw dislocation and the parameters characterizing deviations from the Schmid law have been obtained by *ab initio* calculations in all bcc transition metals: V, Cr, Fe, Nb, Mo, Ta, and W. Deviation of the dislocation trajectory from the average $\{110\}$ slip plane systematically leads to easier glide in the twinning region than in the anti-twinning region. Simple interatomic potentials, like EAM potentials, tend to systematically predict high hard core energies compared to the split core, resulting in large path deviations and large T/AT asymmetries in all bcc metals. By way of contrast, *ab initio* calculations predict a strong metal dependence, with Fe being close to symmetrical and Nb strongly asymmetrical. Variations of the dislocation relaxation volume, responsible for the coupling with non-glide stresses, are also predicted to show highly diverse behaviours among bcc metals. In particular, we found a strong coupling with pressure in Cr and with a tensile stress parallel to the dislocation line in V and Nb. Such

effects cannot be captured by interatomic potentials, whether simple EAM-type potentials or more advanced machine learning potentials, unless the stress variation along the Peierls potential is included in the training set. The versatility and accuracy of *ab initio* calculations was needed to uncover such fine details, which as described in this manuscript, have nonetheless marked consequences on the prediction of the yield stress and slip system activity. It also shows that, contrary to a common simplification used in the literature, all stress components need to be considered when developing a yield criterion for bcc metals.

Development of such a yield criterion for a uniaxial mechanical loading allows comparison with experimental data obtained at low temperatures during tension and compression tests. Despite the overestimation of the Peierls stress inherent to atomistic simulations, which is not resolved by accounting for non-Schmid effects as previously proposed [47], the criterion captures the relative variations of the yield stress with the orientation of the loading axis and manages to predict the active slip systems among all possible $1/2\langle 111 \rangle \{110\}$ systems. It also accounts for the tension/compression asymmetry, predicting how the yield stress varies with the sign of the applied stress. A good agreement is obtained for all bcc metals where such observations exist at low enough temperature, except in regions of the stereographic projection where anomalous slip is reported. But, as summarized by Taylor [4], anomalous slip cannot be explained solely by glide properties of a single dislocation and therefore requires going further than a yield criterion parameterized only on the core properties of the $1/2\langle 111 \rangle$ screw dislocation. Other discrepancies between the present criterion and experimental data may be caused by glide of screw dislocations in planes different from $\{110\}$, most particularly $\{112\}$ planes, even below the athermal temperature of the Peierls mechanism [9, 10], which is not accounted for in this work.

Finally, it is worth pointing that the yield criterion obtained at 0 K can be extended to consider thermal activation and the glide of screw dislocation through nucleation of kink-pairs, using line tension models still parameterized on *ab initio* calculations [29, 36]. Such a generalization in tungsten [20] has shown that non-Schmid effects fade out with increasing temperature and completely disappear only at the athermal temperature where screw dislocations can glide freely without feeling the lat-

tice friction.

Acknowledgments

This work was performed using HPC resources from GENCI-CINES and -TGCC (Grants 2021-096847) and from PRACE through access to Juwels system hosted by Jülich Supercomputing Centre (project DIMAB). BB and EC acknowledge funding by the French Tripartite Institute (CEA-EDF-Framatome) through the ICOMB project. LD acknowledges support from LabEx DAMAS (program "investissements d'Avenir" ANR-11-LABX-008-01).

Appendix A. Elastic constants adjustment

In this section, details are given about the adjustment of the elastic constants performed to ensure that the extracted dislocation positions for the initial and final configurations of the NEB path are lying in the bottom of a Peierls valley and correspond to an easy core, as observed from their differential displacement maps. In the frame of the simulation cell containing the $1/2\langle 111 \rangle$ screw dislocation dipole, the elastic tensor has the following form:

$$\bar{\bar{C}} = \begin{bmatrix} C_{11} & C_{12} & C_{13} & 0 & C_{15} & 0 \\ C_{12} & C_{11} & C_{13} & 0 & -C_{15} & 0 \\ C_{13} & C_{13} & C_{33} & 0 & 0 & 0 \\ 0 & 0 & 0 & C_{44} & 0 & -C_{15} \\ C_{15} & -C_{15} & 0 & 0 & C_{44} & 0 \\ 0 & 0 & 0 & -C_{15} & 0 & C_{66} \end{bmatrix}$$

We use Eq. 1 and only consider the two equations of the system involving the dislocation position $x(\xi)$:

$$\begin{cases} -4 C_{44} b x(\xi) + 4 C_{15} \Delta\Omega_{12}(\xi) = S \Delta\sigma_{23}(\xi) \\ 4 C_{15} b x(\xi) - 4 C_{66} \Delta\Omega_{12}(\xi) = S \Delta\sigma_{12}(\xi) \end{cases}$$

In their final positions, dislocations have glided across one Peierls valley, hence $x(\xi = 1) = \lambda_P$. As both initial and final configurations of the NEB path correspond to the dislocation ground state and are equivalent, $\Delta\Omega_{ij}(\xi = 1) = 0$. One thus should have

$$\begin{cases} -4 C_{44} b \lambda_P = S \Delta\sigma_{23}(\xi = 1) \\ 4 C_{15} b \lambda_P = S \Delta\sigma_{12}(\xi = 1) \end{cases} \quad (\text{A.1})$$

Table A.2: Lattice parameter a_0 (Å), and elastic constants C_{ijkl} (in GPa) rotated in the frame of the $1/2\langle 111 \rangle$ screw dislocation (Perfect crystal), corrected values used to extract the screw dislocation trajectory and relaxation volume (Fit), and values of a simulation containing a dislocation dipole (Dislocated crystal). Adjusted values (C_{15} and C_{44}) are indicated in italic.

	a_0		C_{11}	C_{12}	C_{13}	C_{15}	C_{33}	C_{44}	C_{66}
V	2.998	Perfect crystal	233	163	175	<i>20</i>	221	<i>47</i>	35
		Fit	233	163	175	<i>18</i>	221	<i>48</i>	35
Nb	3.308	Perfect crystal	217	151	164	<i>17</i>	204	<i>42</i>	33
		Fit	217	151	164	<i>15</i>	204	<i>42</i>	33
Ta	3.322	Perfect crystal	288	154	145	<i>-12</i>	296	<i>59</i>	67
		Fit	288	154	145	<i>-9.1</i>	296	<i>55</i>	67
Cr (NM)	2.847	Perfect crystal	420	164	191	<i>38</i>	394	<i>155</i>	128
		Dislocated crystal	416	174	195	<i>33</i>	382	<i>135</i>	118
		Fit	420	164	191	<i>32</i>	394	<i>138</i>	128
Cr (AF)	2.865	Perfect crystal	338	86	117	<i>45</i>	306	<i>157</i>	126
		Fit	338	86	117	<i>35</i>	306	<i>140</i>	126
Mo	3.159	Perfect crystal	416	175	195	<i>27</i>	396	<i>140</i>	120
		Dislocated crystal	413	182	197	<i>22</i>	381	<i>119</i>	115
		Fit	416	175	195	<i>21</i>	396	<i>122</i>	120
W	3.186	Perfect crystal	495	207	211	<i>5.1</i>	492	<i>148</i>	144
		Dislocated crystal	499	213	210	<i>5.4</i>	487	<i>137</i>	143
		Fit	495	207	211	<i>4.5</i>	492	<i>141</i>	144
Fe	2.829	Perfect crystal	320	142	129	<i>-18</i>	333	<i>76</i>	89
		Fit	320	142	129	<i>-17</i>	333	<i>71</i>	89

The elastic constants C_{44} and C_{15} are thus modified to enforce this relation, using the stress differences $\Delta\sigma_{23}(\xi = 1)$ and $\Delta\sigma_{12}(\xi = 1)$ between the initial and final configurations given by *ab initio* calculations.

The values for the rotated bcc unit-cell and the fitted values necessary to ensure both conditions are presented in Tab. A.2. The elastic constants of a simulation cell containing a $1/2\langle 111 \rangle$ screw dislocation dipole are also evaluated for W, Mo, and Cr in the non magnetic (NM) phase, and are presented in the Dislocated crystal row of Tab. A.2. We note that, as already reported for W and Cr, the elastic constants of the dislocated crystal vary by a similar amount from the bulk values as the fitted values chosen to ensure the conditions of Eq. A.1.

Appendix B. Convergence of the parameters of the yield criterion

We present in this section the influence of the number of intermediate images used to interpolate the NEB path for extraction of the parameters of the yield criterion. Calculations are performed for Ta, as the position of the inflexion point of the Peierls enthalpy barrier x^* is located at an extrema

of some components of $\Delta\Omega_{ij}$ (see Fig. 2). The calculation is performed using 5 and 11 intermediate images, with the resulting parameters of the yield criterion given in Tab. B.3.

Table B.3: Convergence of the parameters of the yield criterion with respect to the number of intermediate images of the NEB calculation for Ta: Peiers stress τ_P (GPa), inflexion point of the Peierls enthalpy barrier x^*/λ_P , deviation angle α^* (°), and derivatives of the variation of the relaxation volume $\Delta\Omega'_{ij}$ with respect to x at x^* .

Ta	5 Images	11 Images
τ_P	0.87	0.89
x^*/λ_P	0.083	0.076
α^*	-16.2	-15.8
$\Delta\Omega'_{11}$	-0.288	-0.319
$\Delta\Omega'_{22}$	+0.210	+0.232
$\Delta\Omega'_{33}$	+0.131	+0.146
$\Delta\Omega'_{12}$	-0.095	-0.105

Appendix C. *Ab initio* and experimental yield stresses

Table C.4: Comparison between *ab initio* and experimental yield stresses measured at low temperature. For *ab initio* data, values in roman give the yield stress defined from the maximal slope of the Peierls potential (Eq. 2), *i.e.* $\sigma_Y = 2\tau_P$, while values in italic indicate the minimum and maximum yield stress predicted by the model over the whole stereographic projection (Eqs. 7 and 9). The experimental athermal temperature of the Peierls mechanism T_{ath} and the melting point T_{melt} are reported in the last two columns.

Yield stress σ_Y (MPa)		T_{ath} (K)	T_{melt} (K) [62]	
	<i>Ab initio</i>	Exp.	Exp.	
V	2070 (1 880 – 3 270)	400 [63] (77 K) 350 [64] (77 K) 500 [66] (77 K) 750 [67] (77 K)	300 [63] 450 [65] 400 [64, 67]	2 202
Nb	1 580 (1 380 – 2 370)	900 [61] (4.2 K) 500 – 900 [12] (4.2 K) 600 – 1 200 [70] (4.2 K) 270 – 600 [12] (77 K) 200 – 700 [70, 71] (77 K)	300 [61, 68] 275 – 375 [69]	2 750
Ta	1 750 (1 500 – 2 930)	700 [72] (4.2 K) 500 – 900 [5] (77 K) 470 – 560 [6] (77 K)	400 [52, 73] 400 – 450 [74]	3 293
Cr	NM: 4 640 (4 480 – 7 520) AF: 3 960 (3 730 – 6 450)	970 [75] (77 K) 780 – 1 200 [76] (77 K)	420 [75]	2 133
Mo	2 800 (2 650 – 4 430)	1 140 – 1 600 [12, 14] (4.2 K) 1 620 [77] (4.2 K) 440 – 740 [56] (77 K) 500 – 940 [14] (77 K)	450 [8, 56] 400 – 450 [78]	2 895
W	4 730 (4 330 – 7 680)	1 600 [79] (60 K) 750 – 1 500 [10, 13] (77 K)	800 [79] 600 [80]	3 695
Fe	3 300 (3 180 – 5 880)	720 – 850 [11, 12] (4.2 K) 750 – 950 [81] (4.2 K) 700 [84] (20.4 K) 450 – 550 [85] (60 K) 400 – 500 [11] (77 K)	300 [81] 400 [82, 83]	1 811

References

- [1] J. W. Christian, Some surprising features of the plastic deformation of body-centered cubic metals and alloys, *Metall Mater Trans A* 14 (1983) 1237–1256. doi:10.1007/BF02664806.
- [2] M. S. Duesbery, Z. S. Basinski, On non-glide stresses and their influence on the screw dislocation core in body-centred cubic metals I. The Peierls stress, *Proc. R. Soc. Lond. A* 392 (1984) 145–173. doi:10.1098/rspa.1984.0027.
- [3] R. J. Arsenault, Low Temperature of Deformation of bcc Metals and Their Solid-Solution Alloys, in: *Treatise on Materials Science & Technology*, Vol. 6 of Plastic Deformation of Materials, Elsevier, 1975, pp. 1–99. doi:10.1016/B978-0-12-341806-7.50008-8.
- [4] G. Taylor, Thermally-activated deformation of BCC metals and alloys, *Progress in Materials Science* 36 (1992) 29–61. doi:10.1016/0079-6425(92)90004-Q.
- [5] J. F. Byron, D. Hull, Plastic deformation of tantalum single crystals: I. The surface morphology of yield, *J. Less Common Met.* 13 (1967) 71–84. doi:10.1016/0022-5088(67)90048-3.
- [6] M. H. A. Nawaz, B. L. Mordike, Slip Geometry of Tantalum and Tantalum Alloys, *Phys. Stat. Sol (a)* 32 (1975) 449–458. doi:https://doi.org/10.1002/pssa.2210320213.
- [7] C. R. Weinberger, B. L. Boyce, C. C. Battaile, Slip planes in bcc transition metals, *Int. Mat. Rev.* 58 (2013) 296–314. doi:10.1179/1743280412Y.0000000015.
- [8] T. Suzuki, H. Koizumi, H. O. K. Kirchner, Plastic flow stress of b.c.c. transition metals and the Peierls potential, *Acta Metall.* 43 (1995) 2177–2187. doi:10.1016/0956-7151(94)00451-X.
- [9] D. Caillard, Geometry and kinetics of glide of screw dislocations in tungsten between 95K and 573K, *Acta Mater.* 161 (2018) 21–34. doi:10.1016/j.actamat.2018.09.009.
- [10] A. S. Argon, S. R. Maloof, Plastic deformation of tungsten single crystals at low temperatures, *Acta Metall.* 14 (1966) 1449–1462. doi:10.1016/0001-6160(66)90165-9.
- [11] Y. Aono, E. Kuramoto, K. Kitajima, Plastic deformation of high-purity iron single crystals, *Rep. Res. Inst. Appl. Mech.* 29 (1981) 127–193.
- [12] Y. Aono, E. Kuramoto, K. Kitajima, Orientation dependence of slip in niobium single crystals at 4.2 and 77 K, *Scripta Mater.* 18 (1984) 201–205. doi:10.1016/0036-9748(84)90508-8.
- [13] P. Beardmore, D. Hull, Deformation and fracture of tungsten single crystals, *J. Less Common Met.* 9 (1965) 168–180. doi:10.1016/0022-5088(65)90094-9.
- [14] K. Kitajima, Y. Aono, E. Kuramoto, Slip systems and orientation dependence of yield stress in high purity molybdenum single crystals at 4.2 K and 77 K, *Scripta Metall.* 15 (1981) 919–924. doi:10.1016/0036-9748(81)90278-7.
- [15] L. Dezerald, D. Rodney, E. Clouet, L. Ventelon, F. Willaime, Plastic anisotropy and dislocation trajectory in BCC metals, *Nature Commun.* 7 (2016) 11695. doi:10.1038/ncomms11695.
- [16] A. Kraych, E. Clouet, L. Dezerald, L. Ventelon, F. Willaime, D. Rodney, Non-glide effects and dislocation core fields in BCC metals, *npj Computational Materials* 5 (2019) 1–8. doi:10.1038/s41524-019-0247-3.
- [17] E. Clouet, L. Ventelon, F. Willaime, Dislocation core energies and core fields from first principles, *Phys. Rev. Lett.* 102 (2009) 055502. doi:10.1103/PhysRevLett.102.055502.
- [18] E. Clouet, Dislocation core field. I. Modeling in anisotropic linear elasticity theory, *Phys. Rev. B* 84 (2011) 224111. doi:10.1103/PhysRevB.84.224111.
- [19] E. Clouet, L. Ventelon, F. Willaime, Dislocation core field. II. Screw dislocation in iron, *Phys. Rev. B* 84 (2011) 224107. doi:10.1103/PhysRevB.84.224107.
- [20] E. Clouet, B. Bienvenu, L. Dezerald, D. Rodney, Screw dislocations in BCC transition metals: from ab initio modeling to yield criterion, *Comptes Rendus Physique* 22 (2021) 1–34. doi:10.5802/crphys.75.
- [21] B. Bienvenu, E. Clouet, Ab initio modeling of slip activity in body-centered cubic chromium, *Acta Mat.* 224 (2022) 117485. doi:10.1016/j.actamat.2021.117485.
- [22] G. Kresse, J. Furthmüller, Efficiency of ab-initio total energy calculations for metals and semiconductors using a plane-wave basis set, *Comput. Mater. Sci.* 6 (1996) 15–50. doi:10.1016/0927-0256(96)00008-0.
- [23] J. P. Perdew, K. Burke, M. Ernzerhof, Generalized Gradient Approximation Made Simple, *Phys. Rev. Lett.* 77 (1996) 3865–3868. doi:10.1103/PhysRevLett.77.3865.
- [24] B. Bienvenu, C. C. Fu, E. Clouet, Impact of magnetism on screw dislocations in body-centered cubic chromium, *Acta Mat.* 200 (2020) 570–580. doi:10.1016/j.actamat.2020.09.041.
- [25] L. Casillas-Trujillo, D. Gambino, L. Ventelon, B. Alling, Screw dislocation core structure in the paramagnetic state of bcc iron from first-principles calculations, *Phys. Rev. B* 102 (2020) 094420. doi:10.1103/PhysRevB.102.094420.
- [26] D. Rodney, L. Ventelon, E. Clouet, L. Pizzagalli, F. Willaime, Ab initio modeling of dislocation core properties in metals and semiconductors, *Acta Mat.* 124 (2017) 633–659. doi:10.1016/j.actamat.2016.09.049.
- [27] E. Clouet, Ab initio models of dislocations, in: *Handbook of Materials Modeling : Methods: Theory and Modeling*, Springer International Publishing, 2018, pp. 1–22. doi:10.1007/978-3-319-42913-7_22-1.
- [28] E. Clouet, BABEL software. URL <http://emmanuel.clouet.free.fr/Programs/Babel/index.html>
- [29] L. Dezerald, L. Proville, L. Ventelon, F. Willaime, D. Rodney, First-principles prediction of kink-pair activation enthalpy on screw dislocations in bcc transition metals: V, Nb, Ta, Mo, W, and Fe, *Phys. Rev. B* 91 (2015) 094105. doi:10.1103/PhysRevB.91.094105.
- [30] C. R. Weinberger, G. J. Tucker, S. M. Foiles, Peierls potential of screw dislocations in bcc transition metals: Predictions from density functional theory, *Phys. Rev. B* 87 (2013) 054114. doi:10.1103/PhysRevB.87.054114.
- [31] L. Dezerald, L. Ventelon, E. Clouet, C. Denoual, D. Rodney, F. Willaime, Ab initio modeling of the two-dimensional energy landscape of screw dislocations in bcc transition metals, *Phys. Rev. B* 89 (2014) 024104. doi:10.1103/PhysRevB.89.024104.
- [32] R. Gröger, Which stresses affect the glide of screw dislocations in bcc metals?, *Philos. Mag.* 94 (2014) 2021–2030. doi:10.1080/14786435.2014.904058.
- [33] H. Lim, C. R. Weinberger, C. C. Battaile, T. E. Buchheit, Application of generalized non-Schmid yield law to low-temperature plasticity in bcc transition metals, *Modelling Simul. Mater. Sci. Eng.* 21 (2013) 045015.

- doi:10.1088/0965-0393/21/4/045015.
- [34] A. Koester, A. Ma, A. Hartmaier, Atomistically informed crystal plasticity model for body-centered cubic iron, *Acta Mater.* 60 (2012) 3894–3901. doi:10.1016/j.actamat.2012.03.053.
- [35] G. Po, Y. Cui, D. Rivera, D. Cereceda, T. D. Swinburne, J. Marian, N. Ghoniem, A phenomenological dislocation mobility law for bcc metals, *Acta Mat.* 119 (2016) 123–135. doi:10.1016/j.actamat.2016.08.016.
- [36] L. Proville, L. Ventelon, D. Rodney, Prediction of the kink-pair formation enthalpy on screw dislocations in α -iron by a line tension model parametrized on empirical potentials and first-principles calculations, *Phys. Rev. B* 87 (2013) 144106. doi:10.1103/PhysRevB.87.144106.
- [37] V. Vitek, M. Mrovec, J. L. Bassani, Influence of non-glide stresses on plastic flow: from atomistic to continuum modeling, *Mat. Sci. Eng. A* 365 (2004) 31–37. doi:10.1016/j.msea.2003.09.004.
- [38] R. Gröger, A. G. Bailey, V. Vitek, Multiscale modeling of plastic deformation of molybdenum and tungsten: I. Atomistic studies of the core structure and glide of $1/2 < 111 >$ screw dislocations at 0K, *Acta Mat.* 56 (2008) 5401–5411. doi:10.1016/j.actamat.2008.07.018.
- [39] R. Gröger, V. Racherla, J. L. Bassani, V. Vitek, Multiscale modeling of plastic deformation of molybdenum and tungsten: II. Yield criterion for single crystals based on atomistic studies of glide of $1/2 < 111 >$ screw dislocations, *Acta Mat.* 56 (2008) 5412–5425. doi:10.1016/j.actamat.2008.07.037.
- [40] Z. M. Chen, M. Mrovec, P. Gumbsch, Atomistic aspects of $1/2 < 111 >$ screw dislocation behavior in α -iron and the derivation of microscopic yield criterion, *Modelling Simul. Mater. Sci. Eng.* 21 (2013) 055023. doi:10.1088/0965-0393/21/5/055023.
- [41] R. Gröger, Symmetry-adapted single crystal yield criterion for non-Schmid materials, *Int. J. Plast.* 146 (2021) 103101. doi:10.1016/j.ijplas.2021.103101.
- [42] K. Srivastava, D. Weygand, D. Caillard, P. Gumbsch, Repulsion leads to coupled dislocation motion and extended work hardening in bcc metals, *Nat. Commun.* 11 (2020) 5098. doi:10.1038/s41467-020-18774-1.
- [43] K. Srivastava, R. Gröger, D. Weygand, P. Gumbsch, Dislocation motion in tungsten: Atomistic input to discrete dislocation simulations, *Int. J. Plast.* 47 (2013) 126–142. doi:10.1016/j.ijplas.2013.01.014.
- [44] J. Bressers, P. De Meester, Slip plane choice in vanadium at deformation temperatures $T \leq 0.15 T_m$, *J. Less Common Met.* 84 (1982) 11–23. doi:10.1016/0022-5088(82)90123-0.
- [45] C. Woodward, S. I. Rao, Flexible ab initio boundary conditions: Simulating isolated dislocations in bcc Mo and Ta, *Phys. Rev. Lett.* 88 (2002) 216402. doi:10.1103/PhysRevLett.88.216402.
- [46] L. Proville, D. Rodney, M.-C. Marinica, Quantum effect on thermally activated glide of dislocations, *Nature Mater.* 11 (2012) 845–849. doi:10.1038/nmat3401.
- [47] D. Cereceda, M. Diehl, F. Roters, P. Shanthraj, D. Raabe, J. M. Perlado, J. Marian, Linking atomistic, kinetic Monte Carlo and crystal plasticity simulations of single-crystal tungsten strength, *GAMM-Mitteilungen* 38 (2015) 213–227. doi:10.1002/gamm.201510012.
- [48] D. Cereceda, M. Diehl, F. Roters, D. Raabe, J. M. Perlado, J. Marian, Unraveling the temperature dependence of the yield strength in single-crystal tungsten using atomistically-informed crystal plasticity calculations, *Int. J. Plast.* 78 (2016) 242–265. doi:10.1016/j.ijplas.2015.09.002.
- [49] K. Edagawa, T. Suzuki, S. Takeuchi, Motion of a screw dislocation in a two-dimensional Peierls potential, *Phys. Rev. B* 55 (1997) 6180–6187. doi:10.1103/PhysRevB.55.6180.
- [50] D. Caillard, B. Bienvenu, E. Clouet, Anomalous slip in body-centred cubic metals, submitted (2022).
- [51] K. D. Rogausch, B. L. Mordike, Proc. 2nd Intern. Conf. Strength of Metals and Alloys (1970) 168.
- [52] S. Takeuchi, E. Kuramoto, T. Suzuki, Orientation dependence of slip in tantalum single crystals, *Acta Metall.* 20 (1972) 909–915. doi:10.1016/0001-6160(72)90084-3.
- [53] C. N. Reid, A. Gilbert, G. T. Hahn, Twinning, slip and catastrophic flow in niobium, *Acta Metall.* 14 (1966) 975–983. doi:10.1016/0001-6160(66)90218-5.
- [54] L. N. Chang, G. Taylor, J. W. Christian, Stress asymmetries in the deformation behaviour of niobium single crystals, *Acta Metall.* 31 (1983) 37–42. doi:10.1016/0001-6160(83)90061-5.
- [55] G. L. Webb, R. Gibala, T. E. Mitchell, Interstitial solution hardening and slip asymmetry in tantalum, Inst of Metals, United Kingdom, 1973, iNIS Reference Number: 5124585.
- [56] G. C. Liu, S. S. Lau, J. E. Dorn, The plastic deformation behavior of Mo single crystals under compression, *Phys. Stat. Sol. (a)* 11 (1972) 645–651. doi:https://doi.org/10.1002/pssa.2210110228.
- [57] H. J. Kaufmann, A. Luft, D. Schulze, Deformation mechanism and dislocation structure of high-purity molybdenum single crystals at low temperatures, *Crystal Research and Technology* 19 (1984) 357–372. doi:10.1002/crat.2170190312.
- [58] A. Seeger, L. Hollang, The Flow-Stress Asymmetry of Ultra-Pure Molybdenum Single Crystals, *Materials Transactions, JIM* 41 (2000) 141–151. doi:10.2320/matertrans1989.41.141.
- [59] D. K. Bowen, J. W. Christian, G. Taylor, Deformation properties of niobium single crystals, *Can. J. Phys.* 45 (1967) 903–938. doi:10.1139/p67-069.
- [60] K. J. Bowman, R. Gibala, Stress asymmetry in cyclic deformation of b.c.c. metals, *Acta Metall.* 40 (1992) 193–200. doi:10.1016/0956-7151(92)90213-X.
- [61] S. Takeuchi, T. Hashimoto, K. Maeda, Plastic Deformation of bcc Metal Single Crystals at Very Low Temperatures, *Transactions of the Japan Institute of Metals* 23 (1982) 60–69. doi:10.2320/matertrans1960.23.60.
- [62] C. Kittel, Introduction to solid state physics, Wiley, New York, 1966.
- [63] C. T. Wang, D. W. Bainbridge, The deformation mechanism for high-purity vanadium at low temperatures, *Metall. Mater. Trans. B* 3 (1972) 3161–3165. doi:10.1007/BF02661327.
- [64] T. E. Mitchell, R. J. Fields, R. L. Smialek, Three-stage hardening in vanadium single crystals, *J. Less Common Met.* 20 (1970) 167–170. doi:10.1016/0022-5088(70)90104-9.
- [65] D. L. Harrod, R. E. Gold, Mechanical properties of vanadium and vanadium-base alloys, *Int. Met. Rev.* 25 (1980) 163–222. doi:10.1179/imtr.1980.25.1.163.
- [66] J. Bressers, M. Heerschap, P. De Meester, Deformation properties of vanadium single crystals, *J. Less Common*

- Met. 22 (1970) 321–326. doi:10.1016/0022-5088(70)90082-2.
- [67] H. Yoshinaga, K. Toma, K. Abe, S. Morozumi, The Portevin-Le chatelier effect in vanadium, *Philos. Mag.* 23 (1971) 1387–1403. doi:10.1080/14786437108217009.
- [68] U. Holzwarth, A. Seeger, *Proc. 9th Intern. Conf. Strength of Metals and Alloys* (1991) 577.
- [69] F. Ackermann, H. Mughrabi, A. Seeger, Temperature and strain-rate dependence of the flow stress of ultrapure niobium single crystals in cyclic deformation, *Acta Metall.* 31 (1983) 1353–1366. doi:10.1016/0001-6160(83)90006-8.
- [70] J. Nagakawa, M. Meshii, The deformation of niobium single crystals at temperatures between 77 and 4.2 K, *Philos. Mag. A* 44 (1981) 1165–1191. doi:10.1080/01418618108235801.
- [71] A. J. Garratt-Reed, G. Taylor, Stress-strain curves for niobium crystals deformed at temperatures below ambient, *Philos. Mag.* 33 (1976) 577–590. doi:10.1080/14786437608221120.
- [72] S. Takeuchi, K. Maeda, Slip in high purity tantalum between 0.7 and 40 K, *Acta Metall.* 25 (1977) 1485–1490. doi:10.1016/0001-6160(77)90078-5.
- [73] R. J. Arsenault, An investigation of the mechanism of thermally activated deformation in tantalum and tantalum-base alloys, *Acta Metall.* 14 (1966) 831–838. doi:10.1016/0001-6160(66)90003-4.
- [74] M. Werner, Temperature and strain-rate dependence of the flow stress of ultrapure tantalum single crystals, *Phys. Stat. Sol. (a)* 104 (1987) 63–78. doi:https://doi.org/10.1002/pssa.2211040105.
- [75] M. J. Marcinkowski, H. A. Lipsitt, The plastic deformation of chromium at low temperatures, *Acta Metall.* 10 (1962) 95–111. doi:10.1016/0001-6160(62)90055-X.
- [76] J. Holzer, Z. Chlup, T. Kruml, R. Gröger, Plastic deformation of magnetically isotropic Cr single crystals compressed at 77 K, *Int. J. Plast.* 138 (2021) 102938. doi:10.1016/j.ijplas.2021.102938.
- [77] L. Hollang, M. Hommel, A. Seeger, The Flow Stress of Ultra-High-Purity Molybdenum Single Crystals, *Phys. Stat. Sol. (a)* 160 (1997) 329–354. doi:https://doi.org/10.1002/1521-396X(199704)160:2<329::AID-PSSA329>3.0.CO;2-0.
- [78] F. Guiu, P. L. Pratt, The Effect of Orientation on the Yielding and Flow of Molybdenum Single Crystals, *Phys. Stat. Sol. (b)* 15 (1966) 539–552. doi:10.1002/pssb.19660150214.
- [79] D. Brunner, Temperature dependence of the plastic flow of high-purity tungsten single crystals, *IJMR* 101 (2010) 1003–1013. doi:10.3139/146.110362.
- [80] R. H. Schnitzel, Deformation of tungsten single crystals from 77°C to 800°C, *J. Less Common Met.* 8 (1965) 81–89. doi:10.1016/0022-5088(65)90099-8.
- [81] E. Kuramoto, Y. Aono, K. Kitajima, K. Maeda, S. Takeuchi, Thermally activated slip deformation between 0.7 and 77 K in high-purity iron single crystals, *Philos. Mag. A* 39 (1979) 717–724. doi:10.1080/01418617908239302.
- [82] T. Takeuchi, R. Honda, K. Iwayama, T. Taoka, Tensile Deformation of Iron Single Crystals Having the [100] and [110] Axes between -70°C and 250°C, *Jpn. J. Appl. Phys.* 6 (1967) 1282. doi:10.1143/JJAP.6.1282.
- [83] D. Brunner, J. Diehl, Temperature and Strain-Rate Dependence of the Tensile Flow Stress of High-Purity α -Iron below 250 K. I. Stress/Temperature Regime III, *Phys. Stat. Sol. (a)* 124 (1991) 455–464. doi:https://doi.org/10.1002/pssa.2211240210.
- [84] T. L. Altshuler, J. W. Christian, W. Hume-Rothery, The mechanical properties of pure iron tested in compression over the temperature range 2 to 293°K, *Philos. Trans. R. Soc. Lond. A* 261 (1967) 253–287. doi:10.1098/rsta.1967.0004.
- [85] A. Sato, M. Meshii, Asymmetry in yield stress and irradiation softening of high purity iron single crystals, *Scripta Met.* 8 (1974) 851–859. doi:10.1016/0036-9748(74)90306-8.